Investigation of gap states near conduction band edge in vicinity of interface between Mg-ion-implanted GaN and Al_2O_3 deposited after ultra-high-pressure annealing

Yuki Hatakeyama[1], Tetsuo Narita[2], Michal Bockowski[3, 4], Tetsu Kachi[3], and Masamichi Akazawa[1*]

[1]*Hokkaido University, Kita 13, Nishi 8, Sapporo 060-0813, Japan*

[2]*Toyota Central R&D Labs., Inc., Yokomichi 41-1, Nagakute, Aichi 480-1192, Japan*

[3]*Nagoya University, Furo-cho, Chikusa, Nagoya, Aichi 464-8601, Japan*

[4]*Institute of High Pressure Physics, Sokolowska 29/37, 01-142 Warsaw, Poland*

*E-mail: akazawa@rciqe.hokudai.ac.jp

The gap states near the conduction band edge (E_C) in the vicinity of the interface between Mg-ion-implanted GaN and Al_2O_3 deposited after post-implantation annealing were investigated in the range between E_C–0.15 eV and E_C–0.45 eV. For this purpose, capacitance–voltage measurements were performed on MOS diodes with the *n*-type conduction of Mg-implanted GaN maintained by suppressing the dose. Although the gap state density D_T was reduced for the sample prepared with the dose of 1.5×10^{12} cm^{-2} by conventional rapid thermal annealing (RTA) at 1250 ℃ for 1 min using an AlN protective cap layer, further improvement was achieved by capless ultra-high-pressure annealing (UHPA) at the same temperature for the same duration. Furthermore, the D_T distributions for the samples with capless UHPA at 1400 ℃ for 5 min are comparable to that for the sample with conventional RTA at 1250 ℃ for 1 min using the cap layer.

1. Introduction

Gallium nitride (GaN) has wide bandgap (3.43 eV),[1] high breakdown field (2.3–3.2 MV/cm at a doping density of 1×10^{16}–1×10^{17} cm^{-3}),[2] high electron mobility (1300 $cm^2V^{-1}s^{-1}$),[1] and high saturation electron velocity (2.8×10^7 cm/s).[1] It has been reported by Baliga that the ideal specific on-resistance of GaN vertical power devices is much smaller than that of Si.[3] In addition, excellent properties of GaN MOS structures have been reported in several references.[4–8] Actually, a channel mobility of more than 100 $cm^2V^{-1}s^{-1}$ has been reported for GaN MOSFETs.[9–14] Therefore, GaN can be applied to power MOSFETs that contribute to energy conservation.

To realize high-efficiency and high-power GaN MOSFETs, the establishment of ion implantation technology improves the figure-of-merit up to a level close to the unipolar limit of GaN by reducing the electric field crowding in these devices. For example, vertical double-implanted MOSFETs having a simple structure can be fabricated by selectively doping *n*-type GaN (*n*-GaN) and p-type GaN (*p*-GaN) regions by ion implantation. However, the formation of the *p*-GaN region by ion implantation is a big challenge. Nevertheless, Mg acceptor activation has recently been realized by various high-temperature annealing methods after Mg ion implantation.[15–23] One of the methods is ultra-high-pressure annealing (UHPA) at an ultra-high nitrogen pressure of 1 GPa.[23] This method can achieve a high Mg activation rate owing to the availability of a long-term high-temperature process without significant surface damage generated despite not using a surface protective layer at a high temperature of up to 1480 °C.[23]

From the results of positron annihilation spectroscopy (PAS),[24–26] the dominant point defect generated immediately after Mg ion implantation is the divacancy $V_{Ga}V_N$. According to the electrical measurements of Mg-implanted GaN before annealing, a defect level at 0.25 eV below the conduction band edge (E_C) has been detected.[27–29] This defect level does not disappear after annealing at 500 °C.[27] The combination of electrical measurement and PAS revealed that this discrete defect level at E_C – 0.25 eV was assigned to $V_{Ga}V_N$.[29] Recently, we have found that the E_C – 0.25 eV level disappeared after conventional rapid thermal annealing (RTA) using a protective AlN cap layer at 1250 °C.[30] However, PAS results showed that the divacancies agglomerated to form large clusters at this temperature rather than being fully recovered by AlN cap annealing at similar temperatures.[24] Although annealing at a higher temperature is necessary, surface damage must be prevented. Therefore, the surface analysis of the Mg-implanted GaN should be carried out after annealing. X-ray photoelectron spectroscopy also provided information on the surface after

UHPA at 1400 ℃, which indicated the absence of nitrogen deficits at the annealed surface.[31] Moreover, the electric properties of GaN MOS structures formed after UHPA have been reported for heavily Mg-implanted and nonimplanted samples.[32] However, effects of post-implantation UHPA on the electrical states, *i.e.*, gap states near the surface region, have not been clarified.

The effective mobility and on-resistance of an inversion-type n-channel MOSFET can be affected by the gap states near the GaN surface. In this work, using MOS structures with an Al_2O_3 layer, we investigated the gap states near E_C in the vicinity of the Mg-ion-implanted GaN surface after UHPA. Since the investigation of near-conduction band levels using the MOS structure with *p*-GaN is difficult, we used MOS structures with lightly Mg-implanted *n*-GaN. The effects of UHPA before the fabrication of MOS structures on gap states were investigated for two representative annealing conditions reported for Mg-implanted GaN.

2. Experimental procedure

The MOS diode was prepared as shown in Fig. 1. An *n*-GaN epitaxial layer with a Si donor concentration (N_D) of 5.5×10^{17} cm^{-3} and a thickness of 3 μm was grown by metalorganic vapor phase epitaxy (MOVPE) on a freestanding n^+- GaN (0001) substrate. Mg ions were implanted at an energy of 50 keV and a dose of 1.5×10^{11} or 1.5×10^{12} cm^{-2} with an incident angle of 7° tilted from the normal incidence and with a lateral rotation of 15° from the normal direction to the orientation flat. In the following, each of the dosing concentrations will be referred to as a low or high dose. Mg ions were implanted within a Mg concentration range that does not exceed the concentration of the initially doped Si layer, which was confirmed by secondary ion mass spectrometry (SIMS) as shown in Fig. 2(a). For the *n*-GaN samples with and without Mg ion implantation, UHPA was performed without using a protective cap layer at 1250 ℃ for 1 min or 1400 ℃ for 5 min under a nitrogen pressure of 1 GPa. The former UHPA condition has been chosen because it has been reported that conventional RTA with this condition using a protective cap layer achieved a successful Mg activation,[19–22] while the latter UHPA condition has been reported to achieve a high activation rate.[23] In the high-dose case, the samples subjected to conventional RTA at 1250 ℃ in atmospheric pressure nitrogen flow with a 200-nm-thick AlN cap layer were also prepared. After annealing, the samples were treated with a solution of $HF:H_2O$ = 1:1 prior to the formation of the 30-nm-thick Al_2O_3 layer by atomic layer deposition (ALD) at 300 ℃ using trimethylaluminum and H_2O. The MOS structure

was formed by the electron beam evaporation of the Ni/Au circular top circular electrode (300 μm diameter) and the Ti/Au back ohmic contact. Finally, post-metallization annealing (PMA) was carried out at 300 °C for 3 h in air to reduce the interface state density. According to previous reports,[4, 5] this treatment can efficiently reduce the interface disorder and resultant state densities at the Al_2O_3/GaN interface. We examined the sample before dehydrogenation annealing to clarify the effects of UHPA alone on electrical properties. Indeed, the dehydrogenation of *n*-GaN is difficult, and the reason of this difficulty will be discussed later. Even after capless annealing at 800 °C for as long as 90 min, hydrogen atoms were detected by SIMS, as shown in Fig. 2(b).

To characterize the Al_2O_3/Mg-implanted GaN interface electrically, capacitance–voltage (*C–V*) measurements were performed on the fabricated MOS diodes. The gap state density (D_T) distribution was obtained by the high–low-frequency method[33] from the results of *C–V* measurements. Here, the gap states include interface states and point defect states near the GaN surface.

3. Results and discussion

Figure 3 shows the comparison of *C–V* characteristics among samples (a) without activation annealing (as-implanted), (b) with 1250 °C conventional RTA, and (c) with 1250 °C UHPA. The ideal curve is calculated assuming a constant N_D of 5.0×10^{17} cm^{-3}, which is for setting a reference without taking into account the donor compensation. The solid lines show the *C–V* characteristics under the bias sweep from the negative voltage side to the positive voltage side. The fine black line shows the 1 MHz curve measured under the voltage sweep in the opposite direction to show the hysteresis. For the as-implanted sample in Fig. 3(a), the frequency dispersion is remarkable. The plateau capacitance in the bias voltage range of –13 to –3 V corresponds to the depletion layer width of 150 nm corresponding to the location of the surface Fermi level (E_{FS}) at a deep energy level. Although this is an indication of E_{FS} pinning at the deep point, the frequency dispersion occurring in the relatively high frequency region should have been caused by the response from shallower gap states whose time constant was less than the millisecond order. In the as-implanted sample, the deep depletion layer with a width of ~150 nm should have been caused by the high-density acceptor-like defects, mainly $V_{Ga}V_N$, distributed nonuniformly deep inside the bulk, which has been confirmed by PAS as reported in Ref. 29. Consequently, the plateau capacitance does not reflect the surface potential. Therefore, the information of the pinning position cannot be derived from the capacitance. A detailed

numerical analysis has been reported in Refs. 27 and 28. Thus, the conductance method[33] was used to derive the D_T distribution. On the other hand, the samples annealed at 1250 ℃ showed a much reduced frequency dispersion in the *C–V* characteristics, as shown in Figs. 3(b) and 3(c). In both figures, the wide plateau disappeared. It can be seen in Fig. 3(c) that the least frequency dispersion was achieved by UHPA at 1250 ℃. It is highly likely that D_T was reduced in both samples especially in the UHPA sample. However, the conductance was too small to exactly apply the conductance method. In addition, we should not apply the Terman method[33] here because the doping profile might not be uniform owing to the ion implantation. Actually, a non-uniform doping profile has been derived from the *C–V* curve for the sample with conventional RTA.[30] Therefore, the high–low-frequency method[33] was used to derive the D_T distributions by treating the 1 MHz and 1 kHz *C–V* curves as the high- and low-frequency limits, respectively. In this method, D_T is derived as[33]

$$D_T = \frac{1}{q^2}\left(\left(\frac{1}{C_{LF}} - \frac{1}{C_{OX}}\right)^{-1} - \left(\frac{1}{C_{HF}} - \frac{1}{C_{OX}}\right)^{-1}\right), \quad (1)$$

where C_{LF}, C_{HF}, and C_{OX} are the low-frequency limit, high-frequency limit, and oxide capacitances, respectively. The E_{FS} position from E_C at the bias voltage V is derived as[33]

$$E_C - E_{FS} = -\int_{V_0}^{V}\left(1 - \frac{C_{LF}}{C_{OX}}\right)dV, \quad (2)$$

where V_0 is the voltage for strong accumulation. The applicable energy range of 0.15 – 0.45 eV in the bandgap for use of the 1 MHz and 1 kHz *C–V* curves has been discussed in our previous paper.[30] Briefly, when the measurement frequency is in the range from 1 kHz to 1 MHz, the detection range should be approximately E_C – 0.15 eV to E_C – 0.45 eV assuming that the capture cross section is in the range of 1×10^{-15}–1×10^{-17} cm^{-2}.

The derived D_T distributions are summarized in Fig. 4. The order of the D_T magnitude depending on the samples reflects the order of the frequency dispersion magnitude in Fig. 3. As mentioned above, the discrete level at around E_C – 0.25 eV was detected in the as-implanted sample.[27–29] This level was assigned to the $V_{Ga}V_N$ defects generated by Mg implantation by a combination of electric measurement and PAS.[29] Upon annealing at 1250 ℃, however, this discrete level disappeared and part of the U-shaped distribution was detected in the range from E_C – 0.15 eV to E_C – 0.45 eV. This indicated the reduction in the density of $V_{Ga}V_N$ defects, which is in good agreement with the previously reported PAS

results.[24–26] However, there is a possibility that the agglomeration of these defects as reported in Ref. 24 occurred to generate another defect level outside the present detection energy range rather than a complete removal of vacancy-type defects. UHPA achieved a much reduced interface state density compared with conventional RTA. It is highly likely that UHPA prevented surface damage to a greater extent.

Figure 5 shows a comparison of the *C–V* characteristics of the samples annealed at 1250 °C by UHPA with different doses. Figure 3(c) appears again as Fig. 5(c). For all samples with UHPA, we can see bumps in the *C–V* characteristics. The reason for this will be discussed later. The D_T distributions derived by the high–low-frequency method are summarized in Fig. 6 with the results for the high-dose sample shown in Fig. 4. The implanted samples showed a slightly increased D_T compared with the sample without implantation. During annealing, bulk defects should have diffused toward the surface. Therefore, the surface behaves similar to a sink for defects, as discussed in Ref. 25. The defects may turn into surface disorders. This is a possible reason for the slight increase in D_T in the Mg-ion-implanted samples. There is a possibility that a longer annealing duration might lead to a reduction in D_T in the implanted samples. On the other hand, the D_T distribution of the low-dose sample was located slightly higher than that of the high-dose sample, with a slightly convex upward curve. According to the disorder-induced gap state model, which is a guiding principle for gap states, the interface states due to interface disorders distribute in a continuous U shape in the entire bandgap,[34, 35] while the discrete states can also be detected if the defects exist in the vicinity of the interface.[36, 37] Therefore, a convex upward distribution may indicate the existence of defects near the interface. Possibly, $V_{Ga}V_N$ defects remained owing to the suppression of agglomeration because of the lower density of defects.

Figure 7 shows a comparison of the *C–V* characteristics of the samples with UHPA at 1400 °C. Bumps larger than those of the samples with UHPA at 1250 °C can be seen. The *C–V* characteristics showed that the bumps are due to the donor-like level because the bumps appeared on the negative bias side of the ideal curves.[38] Considering the calculated location of the charge neutral level of E_C – 1.1 eV,[39] it is unlikely caused by the interface states because the interface states should be acceptor-like in the range within 1.0 eV below E_C, where they can respond to the bias sweep at a rate of 50 mV s^{-1}. Therefore, donor-like defects should have existed. A possible cause of the bump appearance is a state related to hydrogen atoms introduced during UHPA.[25, 40–42] Monoatomic interstitial hydrogen (H_i) may have been introduced into *n*-GaN, especially in the near-surface region at a high

density. As shown in Fig. 2(b) for the high-dose sample, we have confirmed by SIMS that hydrogen was not removed even by annealing at 800 °C for 90 min under atmospheric nitrogen pressure after UHPA at 1250 °C for 1 min. In particular, [H] was higher than [Mg], which indicated the existence of H_i. The theoretical calculation in the literature indicated that H_i generated a defect level at E_C – 0.5 eV.[43, 44] This level corresponds to the (+/–) charge transition.[44, 45] Therefore, H_i should have been negatively charged in the *n*-GaN bulk with N_D of 5.0×10^{17} cm^{-3}, which made it difficult to achieve dehydrogenation by annealing because of the very small diffusion coefficient due to the large diffusion barrier in *n*-GaN.[45] A similar phenomenon at the *n*-GaN/*p*-GaN junction has been reported in Refs. 41 and 46.

Owing to the (+/–) charge transition, donor–acceptor transition should be seen in the *C–V* characteristics. The plateau should straddle the ideal curve with a shift towards the positive voltage direction after filling the defects with electrons. Possibly, the absence of this straddling is due to the fact that the broken-line ideal curves in Figs. 3, 5, and 7 are calculated assuming that the uniform doping profile that is the same as that of the as-grown sample without implantation. For a precise investigation, the true ideal *C–V* curve should be calculated considering the effect of the actual charge distribution due to H_i on the doping profile. A detailed numerical analysis is required, which is beyond the scope of this work. As an example, the ideal curve calculated assuming a uniform profile with an increase doping concentration to fit the *C–V* curve at the bottom is added in Fig. 7(b) and shown as the one-dot-chain line, which provides a slightly better explanation. Still, the ideal curves assuming a uniform donor concentration of 5×10^{17} cm^{-3} can be used as a rough benchmark as the first approximation. On the basis of these curves, we found that the capacitances at the *C–V* plateaus of samples with UHPA correspond to 0.6 – 0.7 eV below E_C. Unfortunately, Eq. (2) cannot be applied to these bumps because the energy levels are out of the applicable range. In addition, the depletion layer capacitance is determined by not only the surface potential but also the effective doping concentration. Since the as-implanted sample had the lower effective donor concentration owing to carrier compensation, the plateau capacitance due to E_C – 0.25 eV traps was lower than the bump capacitance owing to donor-like defects at 0.6 – 0.7 eV below E_C after annealing.

According to Ref. 25, H can be trapped by vacancy-type defects upon UHPA at a temperature as low as 1000 °C. At the initial stage of UHPA, the Fermi level in the subsurface region might have located deep inside the bandgap because of the high density of defects. Thus, there is a possibility that mobile H_i^+ was introduced into the implanted

GaN at this stage. However, as the defect density decreased, the Fermi level moved toward E_C in the bulk GaN. Consequently, H_i^+ might have turned into H_i^- and become immobile. Although the bump became larger as the dose increased, the bump was observed even for the sample without implantation. Therefore, there is another way of introducing H_i. At the bare surface of GaN, monoatomic H can be trapped by surface dangling bonds, which might have been another source of H_i. Although SIMS analysis in the near-surface region is difficult owing to surface contamination, H_i might have distributed in the near-surface region of GaN after UHPA.

The D_T distributions derived by the high–low-frequency method are summarized in Fig. 8 for all samples with UHPA at 1400 °C. Even by UHPA at 1400 °C for 5 min, which is the condition for achieving a 70% activation ratio of Mg acceptors,[23] the interface state density is comparable to that for conventional RTA at a lower temperature of 1250 °C. Although the D_T of the sample with conventional RTA might be reduced by optimizing the process for removing the cap layer, post-implantation UHPA achieved improved MOS interface properties even without using a cap layer. Nevertheless, the D_T values of a sample without both Mg ion implantation and UHPA are under the detection limit in the range from E_C – 0.15 eV to E_C – 0.45 eV. Thus, we cannot deny the possibility that the annealing led to an increase of surface disorders resulting in the interface state density included in D_T. In addition, note that D_T increased slightly as the UHPA temperature increased. Therefore, the low annealing temperature is preferable. Still, since no discrete level other than a continuous U-shaped D_T distribution was detected, the increase in D_T did not result from the defects generated by annealing. On the other hand, as mentioned above, the duration of 1 min for UHPA at 1250 °C might have been too short to remove the surface implantation damage. Very recently, long-term UHPA at 1300 °C has been found to be also effective for achieving a high activation ratio.[47, 48] This UHPA condition might also be suitable for reducing D_T. Since the minimum D_T was on the order of 10^{11} cm^{-2} eV^{-1} for all the samples with UHPA, there is a possibility that the optimization of the interface formation process leads to further reduction in D_T.

4. Conclusions

C–V measurements were performed on MOS structures with ALD Al_2O_3 and lightly Mg-ion-implanted *n*-GaN fabricated after UHPA to evaluate the gap states near the conduction band. Although the frequency dispersion and the density of the discrete level at E_C – 0.25 eV assigned to $V_{Ga}V_N$ defects for the high-dose (1.5×10^{12} cm^{-2}) Mg-implanted

samples were reduced by conventional RTA at 1250 ℃ for 1 min, further improved characteristics were achieved by UHPA at the same temperature and for the same duration. The UHPA of the low-dose (1.5×10^{11} cm^{-2}) Mg-implanted sample resulted in a slightly increased D_T with a slightly upward-convex curve, which might indicate that the low density of residual $V_{Ga}V_N$ defects resulted from the incomplete agglomeration. The nonimplanted sample with UHPA at 1250 ℃showed the lowest D_T, which indicated that the defect diffusion toward the surface resulted in a slight increase in the density of surface disorders of implanted samples. Although the D_T distributions for the high-dose, low-dose, and nonimplanted samples with UHPA at 1400 ℃ for 5 min locate higher than those for the samples with UHPA at 1250 ℃ for 1 min, they are comparable to that derived for the sample with conventional RTA at 1250 ℃. The bumps were observed in *C–V* curves for samples with UHPA, which were likely caused by the donor-like level related to H_i that was introduced during UHPA. It is difficult to remove hydrogen from samples subjected to UHPA because of the small diffusion constant in *n*-GaN, which does not matter in *p*-GaN. Since D_T was on the order of 10^{11} – 10^{12} cm^{-2} eV^{-1} or lower, there is a possibility that further improvement of interface properties can be achieved by optimizing annealing conditions and/or interface formation processes.

Acknowledgments

This work was supported by the MEXT programs “Research and development of next-generation semiconductor to realize energy-saving society” (Grant Number JPJ005357) and “Creation of innovative core technology for power electronics” (Grant Number JPJ009777).

References

1) T. Narita and T. Kachi, in *Characterization of Defects and Deep Levels for GaN Power Devices*, eds. T. Narita and T. Kachi, (AIP Publishing, Melville, New York, 2020), "Introduction".
2) T. Maeda, T. Narita, S. Yamada, T. Kachi, T. Kimoto, M. Horita, and J. Suda, J. Appl. Phys. **129**, 185702 (2021).
3) B. J. Baliga, Semicond. Sci. Technol. **28**, 074011 (2013).
4) S. Kaneki, J. Ohira, S. Toiya, Z. Yatabe, J. T. Asubar, T. Hashizume, *Appl. Phys. Lett.* **109**, 162104 (2016).
5) T. Hashizume, S. Kaneki, T. Oyobiki, Y. Ando, S. Sasaki, and K. Nishiguchi, Appl. Phys. Express **11**, 124102 (2018).
6) T. Yamada, D. Terashima, M. Nozaki, H. Yamada, T. Takahashi, M. Shimizu, A. Yoshigoe, T. Hosoi. T. Shimura, H. Watanabe, Jpn. J. Appl. Phys. **58**, SCCD06 (2019).
7) T. Nabatame, E. Maeda, M. Inoue, K. Yuge, M. Hirose, K. Shiozaki, N. Ikeda, T. Ohishi, and A. Ohi, Applied Physics Express **12**, 011009 (2019).
8) D. Kikuta, K. Ito, T. Narita, and T. Kachi, Appl. Phys. Express **13**, 026504 (2020).
9) W. Huang, T. Kahn, and T. P. Chow, IEEE Electron Device Lett. **27**, 796 (2006).
10) H. Otake, K. Chikamatsu, A. Yamaguchi, T. Fujishima, and H. Ohta, Appl. Phys. Express **1**, 011105 (2008).
11) T. Nomura, H. Kambayashi, Y. Niiyama, S. Otomo, and S. Yoshida, Solid-State Electron. **52**, 150 (2008).
12) K. Yamaji, M. Noborio, J. Suda, and T. Kimoto, Jpn. J. Appl. Phys. **47**, 7784 (2008).
13) S. Takashima, K. Ueno, H. Matsuyama, T. Inamoto, M. Edo, T. Takahashi, M. Shimizu, and K. Nakagawa, Appl. Phys. Express **10**, 121004 (2017).
14) D. Ji, W. Li, and S. Chowdhury, IEEE Trans. Electron Devices **65**, 4271 (2018).
15) B. N. Feigelson, T. J. Anderson, M. Abraham, J. A. Freitas, J. K. Hite, C. R. Eddy, F. J. Kub, J. Cryst. Growth **350**, 21 (2012).
16) T. J. Anderson, B. N. Feigelson, F. J. Kub, M. J. Tadjer, K. D. Hobart, M. A. Mastro, J. K. Hite, C. R. Eddy, Electron. Lett. **50**, 197 (2014).
17) J. D. Greenlee, T. J. Anderson, B. N. Feigelson, K. D. Hobart, F. J. Kub, Phys. Status Solidi A **212**, 2772 (2015).

18) T. J. Anderson, J. D. Greenlee, B. N. Feigelson, J. K. Hite, K. D. Hobart, F. J. Kub, IEEE Trans. Semicond. Manuf. **29**, 343 (2016).
19) K. Nomoto, K. Takahashi, T. Oikawa, H. Ogawa, T. Nishimura, T. Mishima, H. G. Xing, T. Nakamura, ECS Trans. **69**, 105 (2015).
20) T. Oikawa, Y. Saijo, S. Kato, T. Mishima, T. Nakamura, Nuclear Instruments and Methods in Physics Research B **365**, 168 (2015).
21) T. Narita, T. Kachi, K. Kataoka, T. Uesugi, Appl. Phys. Exp. **10**, 016501 (2017).
22) T. Niwa, T. Fujii, T. Oka, Appl. Phys. Express **10**, 091002 (2017).
23) H. Sakurai, M. Omori, S. Yamada, Y. Furukawa, H. Suzuki, T. Narita, K. Kataoka, M. Horita, M. Bockowski, J. Suda, and T. Kachi, Appl. Phys. Lett. **115**, 142104 (2019).
24) A. Uedono, S. Takashima, M. Edo, K. Ueno, H. Matsuyama, W. Egger, T. Koschine, C. Hugenschmidt, M. Dickmann, K. Kojima, S.F. Chichibu and S. Ishibashi, Phys. Status Solidi B **255**, 1700521 (2018).
25) A. Uedono, H. Sakurai, T. Narita, K. Sierakowski, M. Bockowski, J. Suda, S. Ishibashi. S. F. Chichibu, and T. Kachi, Sci. Rep. **10**, 17349 (2020).
26) A. Uedono, H. Sakurai, J. Uzuhashi, T. Narita, K. Sierakowski, S. Ishibashi, S. F. Chichibu. M. Bockowski, J. Suda, T. Ohkubo, N. Ikarashi, K. Hono, and T. Kachi, Phys. Status Solidi **259**, 2200183 (2022).
27) M. Akazawa, R. Kamoshida, S. Murai, T. Narita, M. Omori, J. Suda, and T. Kachi, Phys. Status Solidi B **257**, 1900367 (2020).
28) M. Akazawa and R. Kamoshida, Jpn. J. Appl. Phys. **59**, 096502 (2020).
29) M. Akazawa, R. Kamoshida, S. Murai, T. Kachi, and A. Uedono, Jpn. J. Appl. Phys. **60**, 016502 (2021).
30) Y. Hatakeyama and M. Akazawa, AIP Advances **12**, 125224 (2022).
31) M. Akazawa, E. Wu, H. Sakurai, M. Bockowski, T. Narita, and T. Kachi, Jpn. J. Appl. Phys. **60**, 036503 (2021).
32) Y. Wada, H. Mizobata, M. Nozaki, T. Kobayashi, T. Hosoi, T. Kachi, T. Shimura, and H. Watanabe, Appl. Phys. Lett. **120**, 082103 (2022).
33) S. M. Sze and K. K. Ng, *Physics of Semiconductor Devices* (Wiley, Hoboken, NJ, 2007) 3rd ed., Chap. 4.
34) H. Hasegawa and H. Ohno, J. Vac. Sci. & Technol. B **4**, 1130 (1986).
35) H. Hasegawa and M. Akazawa, Appl. Surf. Sci **254**, 8005 (2008).
36) T. Sawada, K. Numata, S. Tohdoh, T. Saitoh and H. Hasegawa, Jpn. J. Appl.

Phys. **32**, 511 (1993).

37) T. Hashizume and R. Nakasaki, Appl. Phys. Lett. **80**, 4564 (2002).

38) M. Miczek, B. Adamowicz, C. Mizue, and T. Hashizume, Jpn. J. Appl. Phys. **48**, 04C092 (2009).

39) W. Mönch, J. Appl. Phys. **80**, 5076 (1966).

40) H. Sakurai, T. Narita, M. Omori, S. Yamada, A. Koura, M. Iwinnska, K. Kataoka, M. Horita, N. Ikarashi, M. Bockowski, J. Suda, and T. Kachi, Appl. Phys. Express **13**, 086501 (2020).

41) T. Narita, H. Sakurai, M. Bockowski, K. Kataoka, J. Suda, and T. Kachi, Appl. Phys. Express **12**, 111005 (2019).

42) K. Hirukawa, K. Sumida, H. Sakurai, H. Fujikura, M. Horita, Y. Otoki, K. Sierakowski, M. Bockowski, T. Kachi, and J. Suda, Appl. Phys. Express **14**, 056501 (2021).

43) J. L. Lyons, A. Janotti, and C. G. Van de Walle, Phys. Rev. Lett. **108**, 156403 (2012).

44) M. Matsubara and E. Bellotti, J. Appl. Phys. **121**, 195702 (2017).

45) S. Limpijumnong and C. G. Van de Walle, Phys. Rev. **68**, 235203 (2003).

46) T. Narita, K. Tomita, S. Yamada, and T. Kachi, Appl. Phys. Express **12**, 011006 (2019).

47) T. Nakashima, E. Kano, K. Kataoka, S. Arai, H. SAkurai, T. Narita, K. Sierakowski, M. Bockowski, M. Nagao, J. Suda, T. Kachi, and N. Ikarashi, Appl. Phys. Express **14**, 011005 (2021).

48) K. Sumida, K. Hirukawa, H. Sakurai, K. Sierakowski, M. Horita, M. Bockowski, T. Kachi, and J. Suda, Appl. Phys. Express **14**, 121004 (2021).

Figure Captions

Fig. 1 Schematic of sample fabrication sequence.

Fig. 2 SIMS results (a) for as-implanted high- and low-dose samples, and (b) for the high-dose sample after annealing at 800 ℃ for 90 min under atmospheric pressure subsequently to UHPA at 1250 ℃. The increase in [H] toward the surface resulted from surface contamination during the SIMS measurement. The [Mg] data in (a) were taken from Figs. 10(a) and 10(b) in our previous paper (Ref. 29).

Fig. 3 *C–V* characteristics of high-dose samples (a) as-implanted, (b) with conventional RTA at 1250 ℃, and (c) with UHPA at 1250 ℃. The data in (a) were taken from Fig. 5(a) in our previous paper (Ref. 29). The data in (b) were taken from Fig. 5(b) in our previous paper (Ref. 30) licensed under CC BY.

Fig. 4 D_T distributions at the ALD Al_2O_3/GaN interface derived from *C–V* characteristics in Fig. 3. The data for the as-implanted sample were taken from Fig. 8 in our previous paper (Ref. 29). The data for the sample with conventional RTA were taken from Fig. 7 in our previous paper (Ref. 30) licensed under CC BY.

Fig. 5 *C–V* characteristics of samples with UHPA at 1250 ℃: (a) Sample without ion implantation, (b) low-dose sample, and (c) high-dose sample [the same plot in Fig. 3 (c) is shown again].

Fig. 6 D_T distributions at ALD Al_2O_3/GaN interface of samples with UHPA at 1250 ℃ derived from *C–V* characteristics shown in Figs. 5 and 3(c).

Fig. 7 *C–V* characteristics of samples with UHPA at 1400 ℃: (a) Sample without ion implantation, (b) low-dose sample, and (c) high-dose sample.

Fig. 8 D_T distributions at ALD Al_2O_3/GaN interface of samples with UHPA at 1400 ℃ derived from *C–V* characteristics shown in Fig. 6.

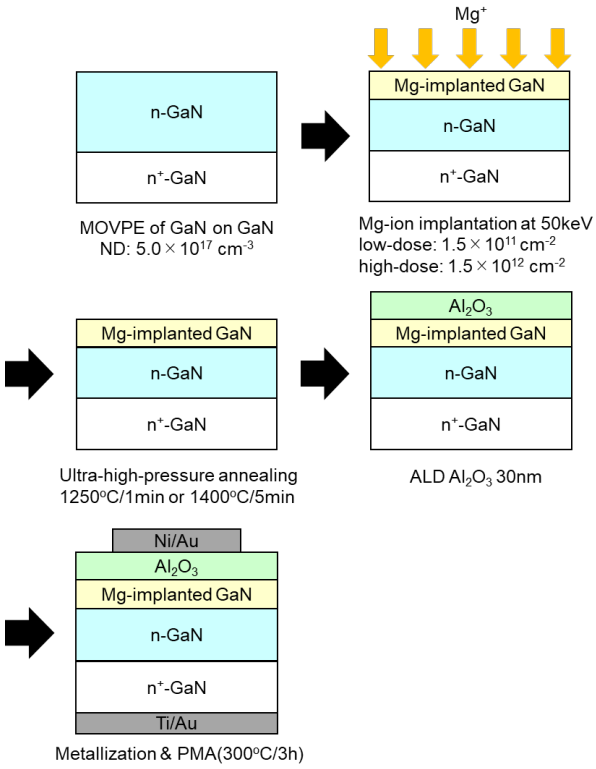
Mg+
n-GaN
n+-GaN
MOVPE of GaN on GaN
ND: 5.0 × 10^17 cm^-3
Mg-implanted GaN
n-GaN
n+-GaN
Mg-ion implantation at 50keV
low-dose: 1.5 × 10^11 cm^-2
high-dose: 1.5 × 10^12 cm^-2
Al2O3
Mg-implanted GaN
n-GaN
n+-GaN
Ultra-high-pressure annealing
1250°C/1min or 1400°C/5min
ALD Al2O3 30nm
Ni/Au
Al2O3
Mg-implanted GaN
n-GaN
n+-GaN
Ti/Au
Metallization & PMA(300°C/3h)

Fig.1

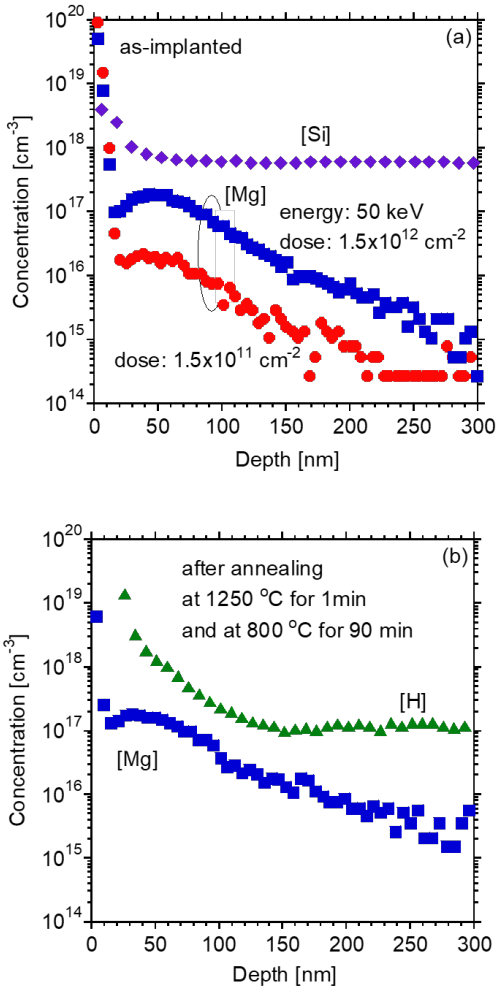
(a)
as-implanted
[Si]
[Mg]
energy: 50 keV
dose: 1.5x10^12 cm^-2
dose: 1.5x10^11 cm^-2
Concentration [cm^-3]
Depth [nm]
(b)
after annealing
at 1250 °C for 1min
and at 800 °C for 90 min
[H]
[Mg]
Concentration [cm^-3]
Depth [nm]

Fig. 2(a)(b)

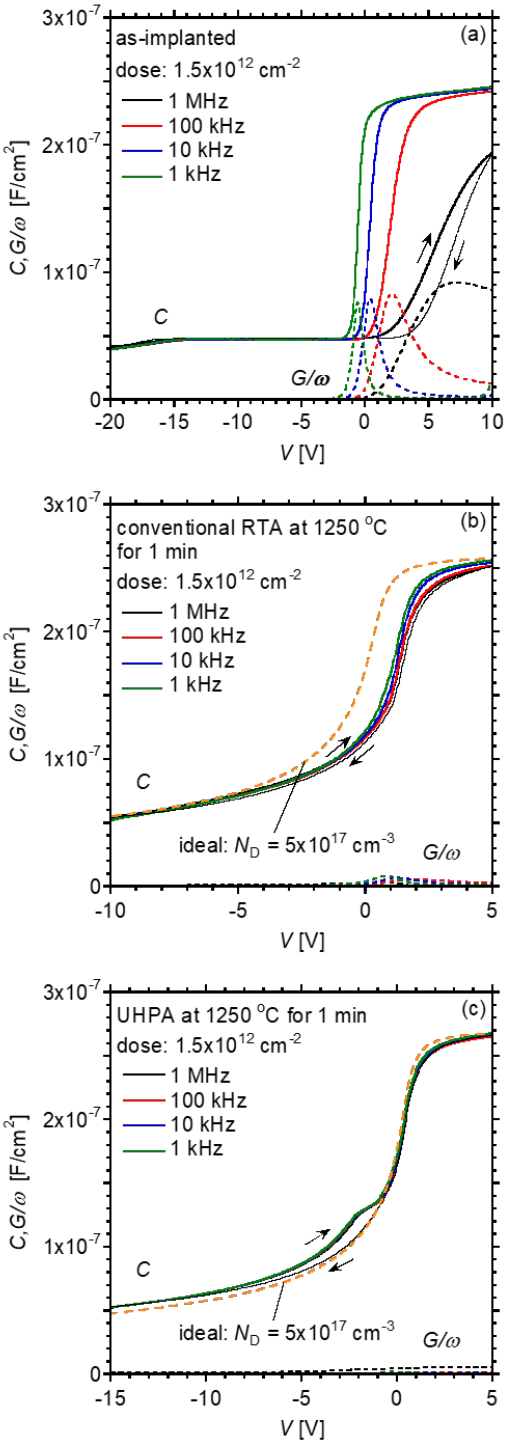
as-implanted
(a)
dose: 1.5x10^12 cm^-2
1 MHz
100 kHz
10 kHz
1 kHz
C
G/ω
C,G/ω [F/cm^2]
V [V]
conventional RTA at 1250 °C
for 1 min
(b)
dose: 1.5x10^12 cm^-2
ideal: N_D = 5x10^17 cm^-3
UHPA at 1250 °C for 1 min
(c)

Fig. 3(a)(b)(c)

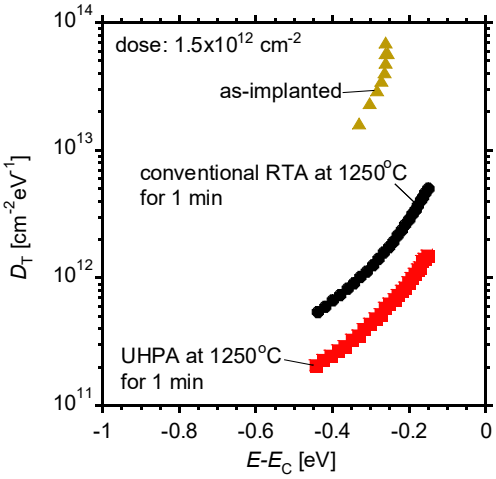
dose: 1.5x10^12 cm^-2
as-implanted
conventional RTA at 1250°C
for 1 min
UHPA at 1250°C
for 1 min
D_T [cm^-2eV^-1]
E-E_C [eV]
10^14
10^13
10^12
10^11
-1
-0.8
-0.6
-0.4
-0.2
0

Fig. 4

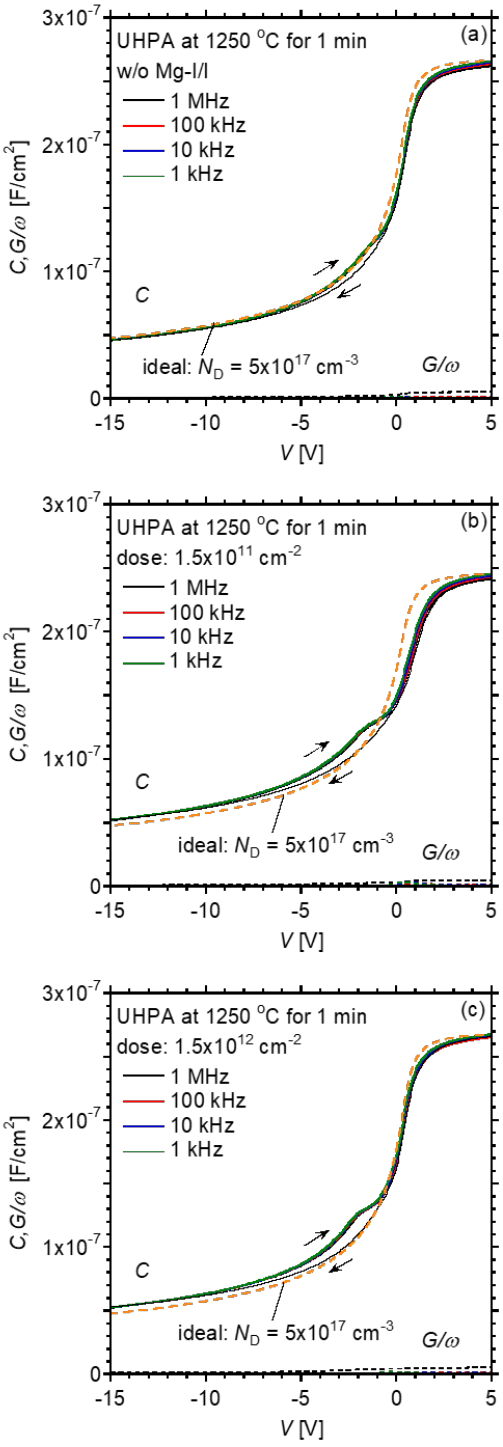
UHPA at 1250 °C for 1 min
w/o Mg-I/I
1 MHz
100 kHz
10 kHz
1 kHz
(a)
C
ideal: N_D = 5x10^{17} cm^{-3}
G/ω
C,G/ω [F/cm^2]
V [V]
UHPA at 1250 °C for 1 min
dose: 1.5x10^{11} cm^{-2}
(b)
UHPA at 1250 °C for 1 min
dose: 1.5x10^{12} cm^{-2}
(c)

Fig. 5(a)(b)(c)

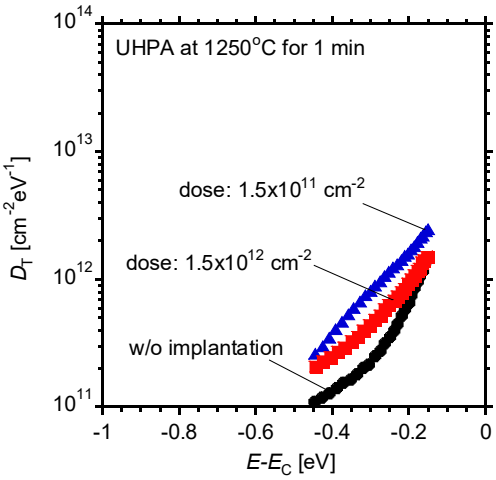
UHPA at 1250°C for 1 min
dose: 1.5x10^11 cm^-2
dose: 1.5x10^12 cm^-2
w/o implantation
D_T [cm^-2eV^-1]
E-E_C [eV]
10^14
10^13
10^12
10^11
-1
-0.8
-0.6
-0.4
-0.2
0

Fig. 6

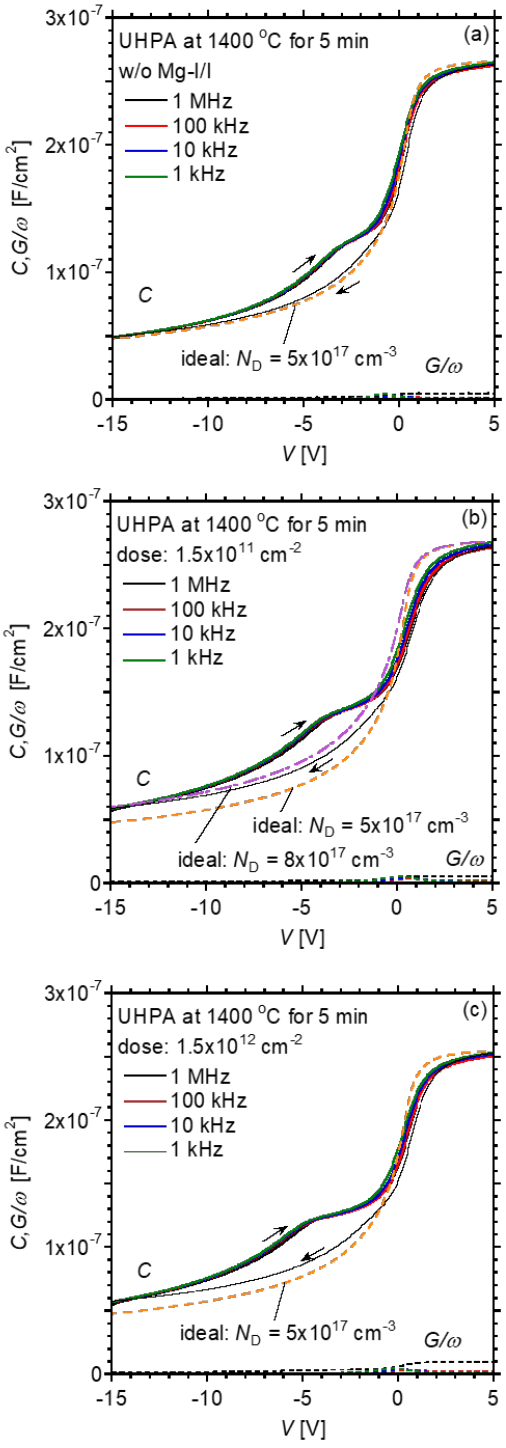
UHPA at 1400 °C for 5 min
w/o Mg-I/I
(a)
1 MHz
100 kHz
10 kHz
1 kHz
C
ideal: N_D = 5x10^{17} cm^{-3}
G/ω
C,G/ω [F/cm^2]
V [V]
UHPA at 1400 °C for 5 min
dose: 1.5x10^{11} cm^{-2}
(b)
ideal: N_D = 8x10^{17} cm^{-3}
UHPA at 1400 °C for 5 min
dose: 1.5x10^{12} cm^{-2}
(c)

Fig. 7(a)(b)(c)

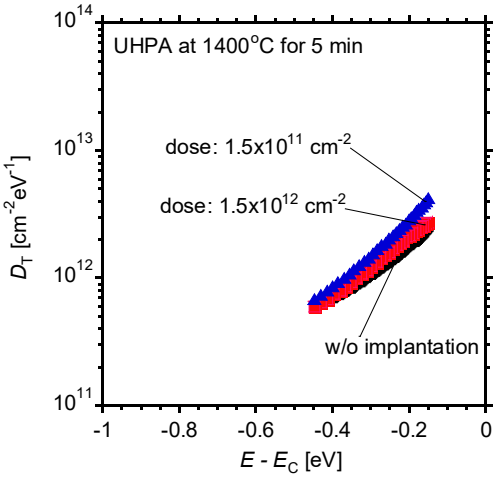
UHPA at 1400°C for 5 min
dose: 1.5x10^11 cm^-2
dose: 1.5x10^12 cm^-2
w/o implantation
D_T [cm^-2eV^-1]
E - E_C [eV]
10^14
10^13
10^12
10^11
-1
-0.8
-0.6
-0.4
-0.2
0

Fig. 8